DØ Note 5974-CONF

Search for neutral Higgs bosons $\phi b \to \tau_e \tau_{had} b$ with 3.7 fb^{-1} of DØ data

The DØ Collaboration
URL http://www-d0.fnal.gov
(Dated: March 15, 2011)

We present the first DØ search for neutral Higgs bosons in the channel $p\bar{p} \to \phi b \to \tau_e \tau_{had} b$. One of the taus is required to decay to an electron and the other decays hadronically. A neural network is used to identify b-quark jets and two multivariate techniques are employed to separate the signals from the main backgrounds: multijets and $t\bar{t}$ events. We set limits on the ϕb production cross section times branching ratio for Higgs boson masses between 90 and 300 GeV, based on 3.7 fb^{-1} of DØ data.

Preliminary Results for Winter 2011 Conferences

I. INTRODUCTION

In models of Supersymmetry, the Higgs sector has two doublets which couple to up and down type fermions. After spontaneous symmetry breaking, five physical Higgs bosons remain: two charged $H^{\pm}$, two CP-even neutral scalars H (heavier) and h (lighter), and a CP-odd neutral pseudoscalar A. Supersymmetry constrains at tree level the masses and couplings of all five Higgs bosons, which can be determined by two independent parameters, usually the mass of the CP-odd pseudoscalar m_A and the ratio of vacuum expectation values of the neutral Higgs fields $\tan\beta$. In this note we refer to all three supersymmetric neutral Higgs bosons by $\phi = h, H, A$, and may refer to ϕ or any of h, H, A interchangeably.

Neutral Higgs bosons can be produced at the Tevatron through the processes $p\bar{p} \to \phi$ and $p\bar{p} \to \phi + b$. In the Minimal Supersymmetric Standard Model (MSSM) [1], the ϕ production cross section is proportional to $\tan^2\beta$ and it is thus enhanced to a few pb for large ($\tan\beta \gtrsim 10$) values. The main decay modes of ϕ Higgs bosons are to $b\bar{b}$ ($\sim$90% of branching fraction) and to $\tau\bar{\tau}$ ($\sim$10%). The $p\bar{p} \to \phi b \to b\bar{b}b$ final state offers a large branching fraction but suffers from large multijet backgrounds. On the other hand, the $\tau\bar{\tau}b$ final state has a smaller branching fraction but is easier to identify from the backgrounds, offering a similar sensitivity in the end.

In this note we present the first DØ results on the decay mode $p\bar{p} \to \phi b \to \tau_{\rm e}\tau_{\rm had}b$, where the final state includes an electron from a τ decay, a hadronic τ, and a jet identified as a b-quark jet. This analysis has been designed to complement the existing $\tau_\mu\tau_{\rm had}b$ search [2], and uses many of the techniques developed there. It will also form part of the combination of all production and decay modes studied in DØ [3]. CDF has published results on supersymmetric neutral Higgs boson production in inclusive di-tau decays, but not explicitly identifying a b-jet [4].

II. DØ DETECTOR

The DØ detector has a central-tracking system, consisting of a silicon microstrip tracker (SMT) and a central fiber tracker (CFT), both located within a 2 T superconducting solenoidal magnet [5], with designs optimized for tracking and vertexing at pseudorapidities $|\eta| < 3$ and $|\eta| < 2.5$, respectively [24]. A liquid-argon and uranium calorimeter has a central section (CC) covering pseudorapidities $|\eta|$ up to ≈ 1.1, and two end calorimeters (EC) that extend coverage to $|\eta| \approx 4.2$, with all three housed in separate cryostats [6]. Each calorimeter contains an electromagnetic (EM) section closest to the interaction region with approximately 20 radiation lengths of material, followed by fine and coarse hadronic sections with approximately six nuclear interaction lengths. An outer muon system, at $|\eta| < 2$, consists of a layer of tracking detectors and scintillation trigger counters in front of 1.8 T toroids, followed by two similar layers after the toroids [7]. Luminosity is measured using plastic scintillator arrays placed in front of the EC cryostats. The trigger and data acquisition systems are designed to accommodate the high luminosities of Run II.

In the spring of 2006, a new inner layer was added to the silicon vertex detector to compensate for expected radiation-induced degradation of the original silicon detector, and the trigger system was improved to handle the increased instantaneous luminosity of the Tevatron.

III. DATA SET AND SIMULATED SAMPLES

The data used in this analysis were recorded between April 2002 and February 2006 (RunIIa) and June 2006 and September 2008 (RunIIb). The total luminosity for this analysis after data quality selection is approximately 3.7 fb^{-1}. Data events are selected online by requiring either a single electron candidate, or an electron candidate and at least one jet candidate. Backgrounds are estimated from simulated events and from a data sample orthogonal with the signal sample. Z+jets, W+jets, and $t\bar{t}$ samples were generated with ALPGEN [8], using PYTHIA [9] for hadronization and showering. Diboson (WW, WZ, and ZZ) samples were generated with PYTHIA with the CTEQ6L1 parton distribution functions [10]. The TAUOLA [11] program is used to model tau decay and EVTGEN [12] is used to decay b hadrons. The generator outputs are passed through a detailed detector simulation based on GEANT [13]. The multijets background, where the electron and hadronic tau arise from jet misidentification, is derived from the data (Sec. IV A).

The signal samples are generated using PYTHIA for the Standard Model process $hb \to \tau\tau b + X$, using Higgs boson masses from 90 to 200 GeV in 10 GeV intervals, and from 200 to 300 GeV in 20 GeV intervals. Neutral SUSY Higgs bosons behave very similarly to Standard Model (SM) Higgs bosons and are degenerate in mass in the 90-160 GeV region. The leading order production by PYTHIA is corrected with next-to-leading order effects by reweighting the signal with MCFM [14] kinematics as a function of the $p_{\rm T}$ and η of the leading b quark in each event.

All simulated samples are normalized using the theoretical cross section for the process and the luminosity of the data sample. The simulated samples include an overlay of minimum bias data with an instantaneous luminosity profile adjusted to match that of the data. The simulated primary vertex longitudinal position is also corrected based on fits

to data at different luminosities. The trigger and electron identification efficiencies in the simulation are corrected for differences between data and the simulation.

The simulated Z+jets samples are reweighted as a function of the $p_{\rm T}(Z)$ and jet multiplicity to correctly describe the $p_{\rm T}(Z)$ spectrum in the data. These corrections are derived from $Z \to ee$ data. We apply an additional factor of 1.67 for $Zc\bar{c}$, 1.52 for $Zb\bar{b}$, and 1.47 for $Wc\bar{c}$ and $Wb\bar{b}$ to take into account NNLO heavy-quark enhancement [15]. This results in acceptable agreement between data and simulation in dedicated W/Z+jets samples.

IV. EVENT SELECTION

The final state we are interested in contains one electron, one hadronic τ, and a b-jet. We required one electron in the event with $p_{\rm T}$ > 15 GeV and $|\eta| < 1.1$ or $1.5 < |\eta| < 2.5$. The electron candidate has a track match, its energy deposition is consistent with that of an electron shower, and is isolated from other energy depositions in the calorimeter. We vetoed any other electrons of this kind (to reject $Z \to ee$ events), and muons (to not overlap with the $\tau_\mu \tau_{\rm had} b$ channel search). The selected electron must be matched to the electron candidate that triggered the event.

Hadronic tau decays are identified in DØ according to three categories, depending on the number of tracks and the electromagnetic calorimeter (EM) energy:

- Type 1: A calorimeter object with no EM subclusters and one charged track. This corresponds to the decay $\tau \to \pi^{\pm}\nu$
- Type 2: A calorimeter object with at least one EM subcluster and one charged track. This corresponds to $\tau \to \pi^{\pm}\pi^0\nu$
- Type 3: A calorimeter object with at least two charged tracks (with or without EM subclusters). This corresponds to $\tau^{\pm} \to \pi^{\pm}\pi^{\pm}\pi^{\mp}\nu$ ...

We required one hadronic tau candidate with the following kinematic selection on the $E_{\rm T}$ and associated track $p_{\rm T}$. For type 1, $E_{\rm T} > 10$ GeV, $p_{\rm T}^{\rm trk} > 15$ GeV; for type 2, $E_{\rm T} > 5$ GeV, $p_{\rm T}^{\rm trk} > 5$ GeV; and for type 3, $E_{\rm T} > 10$ GeV, $p_{\rm T}^{\rm trk} > 5$ GeV, $\sum p_{\rm T}^{\rm trk} > 7$ GeV. A neural network (NN_τ) [16], trained to distinguish taus from jets, is also used to improve the purity of the selected τ candidates. We required: $NN_\tau > 0.9$ for types 1 and 2, and $NN_\tau > 0.95$ for type 3. A second neural network (NN_e), trained to distinguish type 2 taus from electrons, is also used to further reduce the $Z \to ee$ background: $NN_e > 0.9$ (for type 2 taus only). The tau candidate has to be separated from the electron by $\Delta R(e,\tau) > 1.0$ [25], and have opposite charge. The EMF of the tau candidate (the ratio of the energy deposited in the EM calorimeter to the total energy deposited in both EM and hadronic calorimeters) must be less that 0.9 for type 2 and 3 taus. Finally, we applied a correction to the simulated tau energy to ensure that the calorimeter energy and the track $p_{\rm T}$ ratio ($E_{\rm T}/p_{\rm T}^{\rm trk}$) distributions matched the data in $Z \to \tau\tau$ events.

After the electron and the tau candidates have been selected, we required at least one good jet in the event, with $p_{\rm T}$ > 15 GeV and $|\eta| < 2.5$. Jets in the simulated samples need to be corrected for differences in the reconstruction and identification efficiency, for the worse energy resolution in the data than in the simulation, and for different calorimeter responses. All jets are required to be isolated from the selected electron $\Delta R(e, {\rm jet}) > 0.5$, and from the hadronic tau candidate $\Delta R(\tau, {\rm jet}) > 0.5$. Jets are allowed to contain muons inside a cone of 0.5 radius in ΔR.

A. Instrumental background estimation

We expect a large contribution from light- and heavy- flavor multijet events (QCD). These are poorly described in the simulation, so the contribution is estimated from the data. Since the signal tau ID requires $NN_\tau > 0.9$ to distinguish taus from jets, an orthogonal QCD-enriched sample is obtained requiring that the tau is jet-like ($0.3 < NN_\tau < 0.8$) and that the electron is only loosely isolated. This reduces the contribution from $Z \to \tau\tau$ and ensures that the QCD enriched sample is orthogonal with the signal sample.

The contribution from QCD should have approximately equal amounts of electron-tau same-sign (SS) and opposite-sign (OS) events. We can estimate the number of QCD events in the signal region OS by subtracting the number of SS non-QCD background events from the SS signal data events, and correcting it for the fraction of OS to SS events

in the enriched QCD sample ($f_{\rm QCD}$):

$$N^{\rm SS}_{\rm QCD}({\rm signal}) = N^{\rm SS}_{\rm data}({\rm signal}) - N^{\rm SS}_{\rm bkg}({\rm signal}) \quad (1)$$

$$N^{\rm OS}_{\rm QCD}({\rm signal}) = f_{\rm QCD} \times [N^{\rm SS}_{\rm data}({\rm signal}) - N^{\rm SS}_{\rm bkg}({\rm signal})] \quad (2)$$

$$f_{\rm QCD} = \frac{N^{\rm OS}_{\rm data}({\rm QCDrich}) - N^{\rm OS}_{\rm bkg}({\rm QCDrich})}{N^{\rm SS}_{\rm data}({\rm QCDrich}) - N^{\rm SS}_{\rm bkg}({\rm QCDrich})} \quad (3)$$

where "signal" refers to the signal selection sample and "QCDrich" refers to the enriched QCD selection sample, "data" is the observed data yield and "bkg" is the yield from the sum of simulated backgrounds. The QCD OS/SS ratios are shown in Table I.

Type	RunIIa $f_{\rm QCD}$	RunIIb $f_{\rm QCD}$
1	1.08 ± 0.10	1.02 ± 0.04
2	1.05 ± 0.04	1.01 ± 0.02
3	1.03 ± 0.02	1.02 ± 0.01

TABLE I: $f_{\rm QCD}$ scale factor by τ type for QCD estimation, for the two main datasets in the analysis RunIIa (1.1 fb^{-1}) and RunIIb (2.6 fb^{-1}). Errors are statistical only.

This method allows one to obtain both the number of estimated multijet events and the distribution of events.

B. Yields and distributions after selection

Table II shows the number of selected data and predicted background events after selection, as a function of tau type. Figure 1 shows some kinematic variables. These plots contain the result of a Kolmogorov-Smirnov (KS) test comparing the data to the prediction, showing good agreement.

Source	Type 1	Type 2	Type 3	All Types
m_h= 90 GeV	1.5 ± 0.1	4.3 ± 0.2	4.0 ± 0.2	9.8 ± 0.4
Multijet	103.3 ± 9.7	575.3 ± 22.7	822.8 ± 26.5	1501.3 ± 36.2
$Z \to \tau\tau$	82.9 ± 1.3	271.3 ± 2.1	226.8 ± 2.1	580.9 ± 3.3
$Z \to$ ee	6.9 ± 0.5	48.1 ± 1.3	46.9 ± 1.0	101.9 ± 1.7
W+jets	30.5 ± 1.1	134.6 ± 2.3	262.4 ± 3.1	427.4 ± 4.0
Diboson	1.8 ± 0.1	8.3 ± 0.2	13.1 ± 0.3	23.2 ± 0.4
$t\bar{t}$	2.2 ± 0.0	11.4 ± 0.1	12.3 ± 0.1	26.0 ± 0.1
Background Sum	227.5 ± 9.9	1049.0 ± 22.9	1384.3 ± 26.8	2660.8 ± 36.6
Data	223	1041	1365	2629

TABLE II: Number of selected events in 3.7 fb^{-1}, before b-tagging. The signal corresponds to m_h= 90 GeV and has been normalized to $\sigma\times$BF = 1 pb. The uncertainties are statistical only.

V. YIELDS AND DISTRIBUTIONS AFTER b-TAGGING

The final requirement consists in selecting events where one of the jets is identified as originating from a b-quark. We employ a Neural Network (NN_b) [17] cut to separate b-jets from light and gluon jets, with typical b-tag efficiencies of around 50% and fake rates of around 0.8%. In the data, we run the tagger directly and apply the NN_b cut. In the simulation, depending on the flavor of each jet, we apply a Tag Rate Function (TRF) that is corrected for the difference in efficiency of the tagger to identify b-, c- and light-quarks between the data and the simulation. The TRFs return a probability that that particular jet is tagged. We combine the probabilities for each jet in the event as an event weight. The multijet background is estimated after b-tagging using Eq. 1 where the data and background samples are now after b-tagging.

The yields after b-tagging are shown in Table III. After b-tagging, the sample is dominated by multijet (55% of the total background prediction) and $t\bar{t}$ (20%). Figures 2 and 4 show some kinematic distributions after b-tagging.

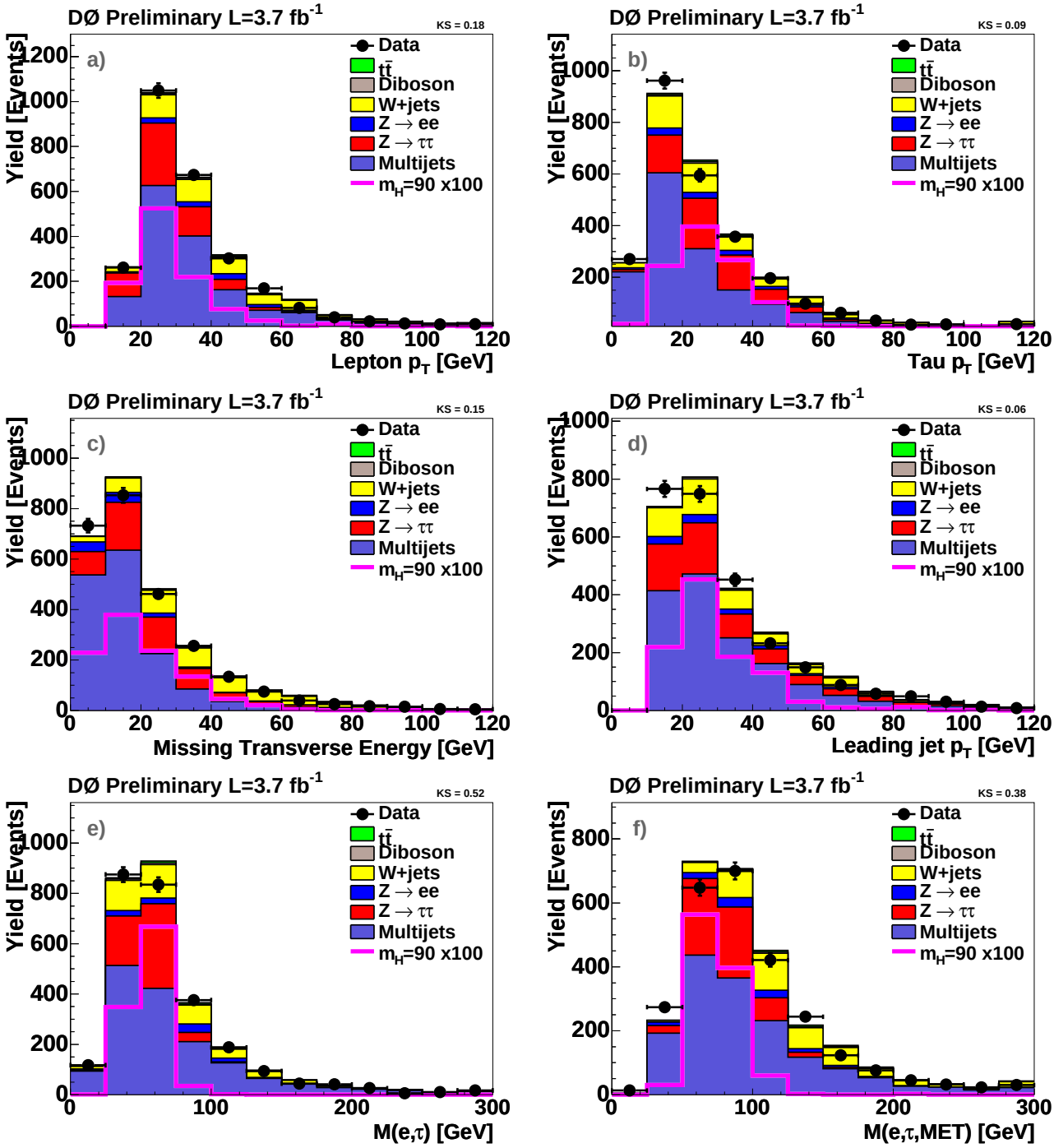

FIG. 1: Kinematic variables after selection and before b-tagging. The electron p_{T} (a), the tau p_{T} (b), the missing transverse energy MET (c), the leading jet p_{T} (d), the invariant mass of the electron and tau (e), and the invariant mass of the electron, tau and MET (f).All tau types are combined.

VI. MULTIVARIATE ANALYSIS

There is not a single variable where it would be easy to cut to extract a clear signal from the large backgrounds. Therefore, we have utilized the same two multivariate methods derived in the $\tau_\mu \tau_{\mathrm{had}} b$ channel search [2] to fight the main two backgrounds: multijet and $t\bar{t}$.

Source	Type 1	Type 2	Type 3	All Types
m_h=90 GeV	0.52 ± 0.04	1.52 ± 0.07	1.25 ± 0.07	3.28 ± 0.11
Multijet	1.95 ± 1.38	16.11 ± 3.91	21.55 ± 4.40	39.61 ± 6.04
$Z \to \tau\tau$	1.33 ± 0.02	4.18 ± 0.02	3.35 ± 0.02	8.85 ± 0.04
$Z \to$ ee	0.08 ± 0.00	0.80 ± 0.02	0.71 ± 0.01	1.58 ± 0.02
W+jets	0.38 ± 0.01	1.75 ± 0.03	4.24 ± 0.05	6.37 ± 0.06
Diboson	0.04 ± 0.00	0.23 ± 0.01	0.37 ± 0.01	0.65 ± 0.01
$t\bar{t}$	1.32 ± 0.02	6.62 ± 0.04	7.00 ± 0.05	14.94 ± 0.06
Background Sum	5.10 ± 1.38	29.68 ± 3.91	37.22 ± 4.40	72.00 ± 6.04
Data	4	28	29	61

TABLE III: Number of selected events in 3.7 fb^{-1}, after b-tagging. The signal corresponds to m_h= 90 GeV and has been normalized to $\sigma\times$BF = 1 pb. The uncertainties are statistical only.

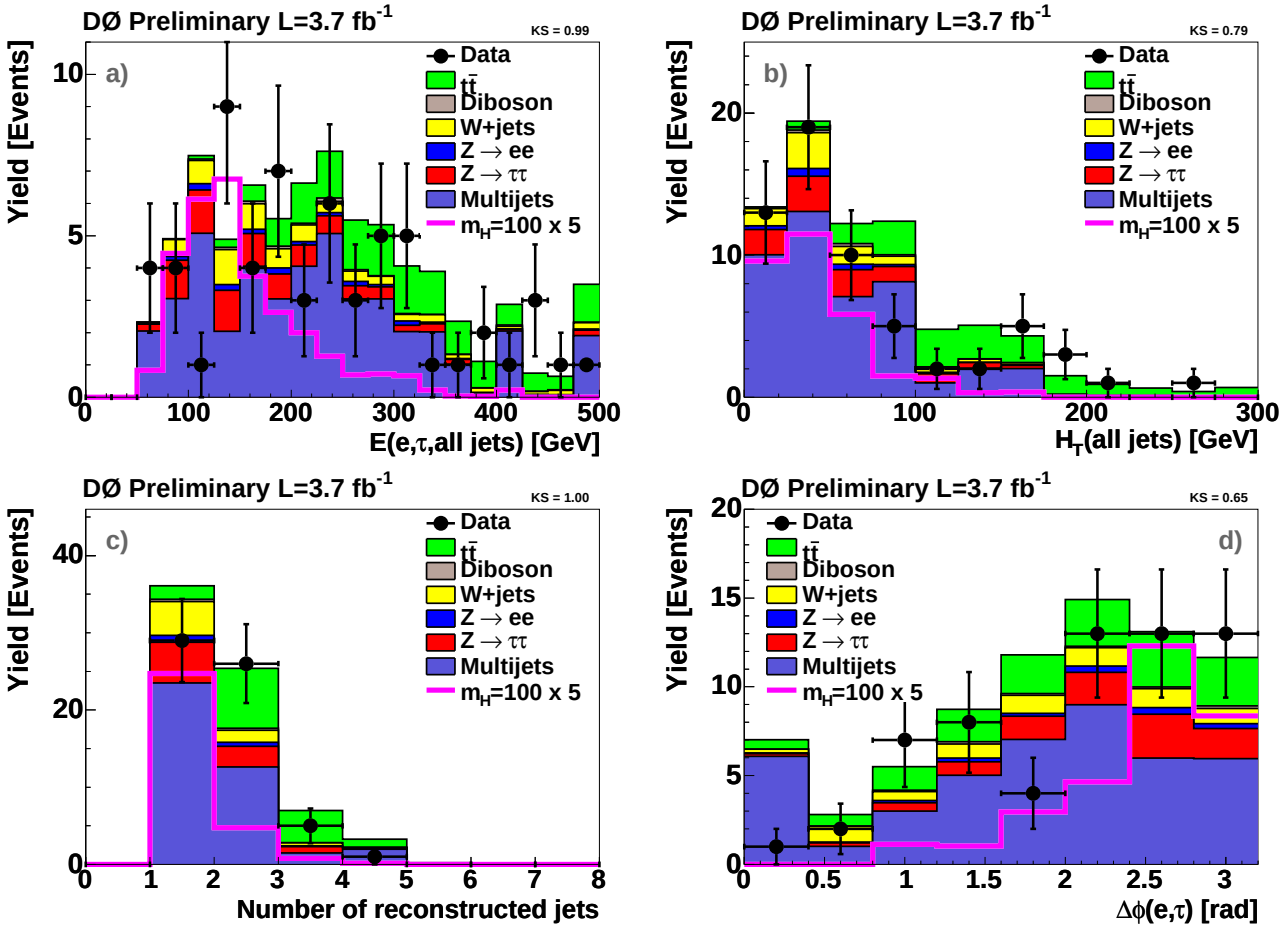

FIG. 2: $NN_{\rm top}$ input variables after b-tagging. All tau types are combined.

A. Neural Network against $t\bar{t}$

To reject $t\bar{t}$ background, we apply the same Kinematic Neural Network ($NN_{\rm top}$) developed for [2]. The $NN_{\rm top}$ takes as inputs four variables, chosen because the kinematics of the signal and the $t\bar{t}$ events is different in them: i) the $H_{\rm T}$ (scalar sum of $p_{\rm T}$) of all jets in the event (excluding the tau); ii) the energy of the four-vector sum of the tau, electron and all jets in the event; iii) the number of jets in the event; and iv) the $\Delta\phi(e,\tau)$.

The separation between background and signal of the $NN_{\rm top}$ can be seen in Figure 3.

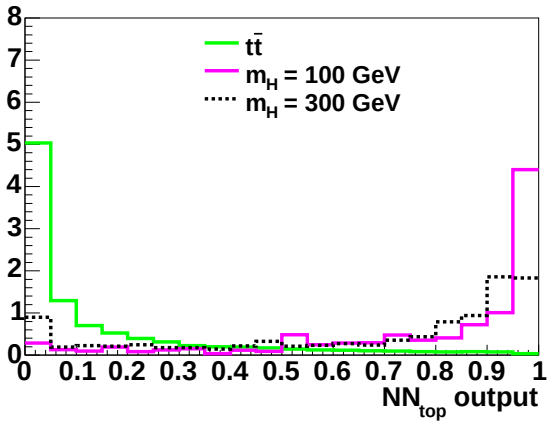

FIG. 3: $NN_{\rm top}$ separation between low- and high-mass signal and $t\bar{t}$ background, for all tau types combined. All areas are normalized to 10.

B. Likelihood probability against multijet

To reject the main background, multijet events, an unbinned likelihood ratio technique ($LL_{\rm MJ}$ hereafter) was developed in the muon decay channel [2] and we have adopted it here. The $LL_{\rm MJ}$ builds a probability that a given event is signal-like or background-like, based on the templates of several discriminant variables. We use the same five input variables used in the muon channel: i) electron $p_{\rm T}$; ii) tau $p_{\rm T}$; iii) $\Delta R(e,\tau)$; iv) invariant mass of the electron-tau pair $M_{e\tau}$; and v) the visible mass $M_{\rm vis} = M_{e,\tau,\not\!\!E_{\rm T}}$. The templates are obtained for this analysis from the selected signal samples at the different mass points and the multijet distributions before b-tagging, due to the small statistics of events after b-tagging. Figure 4 shows the agreement between data and predicted backgrounds after b-tagging for the $LL_{\rm MJ}$ input variables.

The likelihood of an event to be multijet-like or signal-like is computed in all five variables. The $LL_{\rm MJ}$ is defined as the logarithm of the ratio of the signal likelihood to multijet likelihood. Thus signal events tend to have high values and multijet events tend to have low values. We constrain the $LL_{\rm MJ}$ output to be between -10 and 10. The separation between background and signal can be seen in Figure 5. We observe that for low signal masses, as can been on the left panel in Fig. 5, the separation of the multijet background is very poor. Signal like events peak at around $LL_{\rm MJ}$=5 and background events peak below 0, but the kinematics of the low-mass signal is very similar to that of multijet events. The separation improves for high Higgs boson masses, where most of the signal is above $LL_{\rm MJ}$=0.

C. Combined discriminant variable

Finally, in order to derive a cross section limit, we use a one-dimensional variable that combines the separation gained from the $NN_{\rm top}$ and the $LL_{\rm MJ}$:

$$\frac{LL_{\rm MJ}+10}{20} \times NN_{\rm top}\ . \tag{4}$$

The factors 10 and 20 are there to ensure that the $LL_{\rm MJ}$ is bound between 0 and 1, just as the $NN_{\rm top}$ is. So this final variable is also bound between 0 and 1. Figure 6 shows the separation between the main two backgrounds and the signal for the combined variable trained with 100 and 300 GeV Higgs bosons. Figure 7 shows the data and background prediction for two combined variable discriminants after b-tagging, trained for low and high mass Higgs bosons.

VII. SYSTEMATIC UNCERTAINTIES

The sources of systematic uncertainty in this preliminary analysis include the Jet Energy Scale (JES), the jet identification efficiency (JetID), the jet resolution (JetRes), the b-tag efficiency, the trigger efficiency, tau identification, tau energy scale, electron identification, luminosity, normalization cross sections, and multijet background estimation. The different uncertainties are calculated as follows:

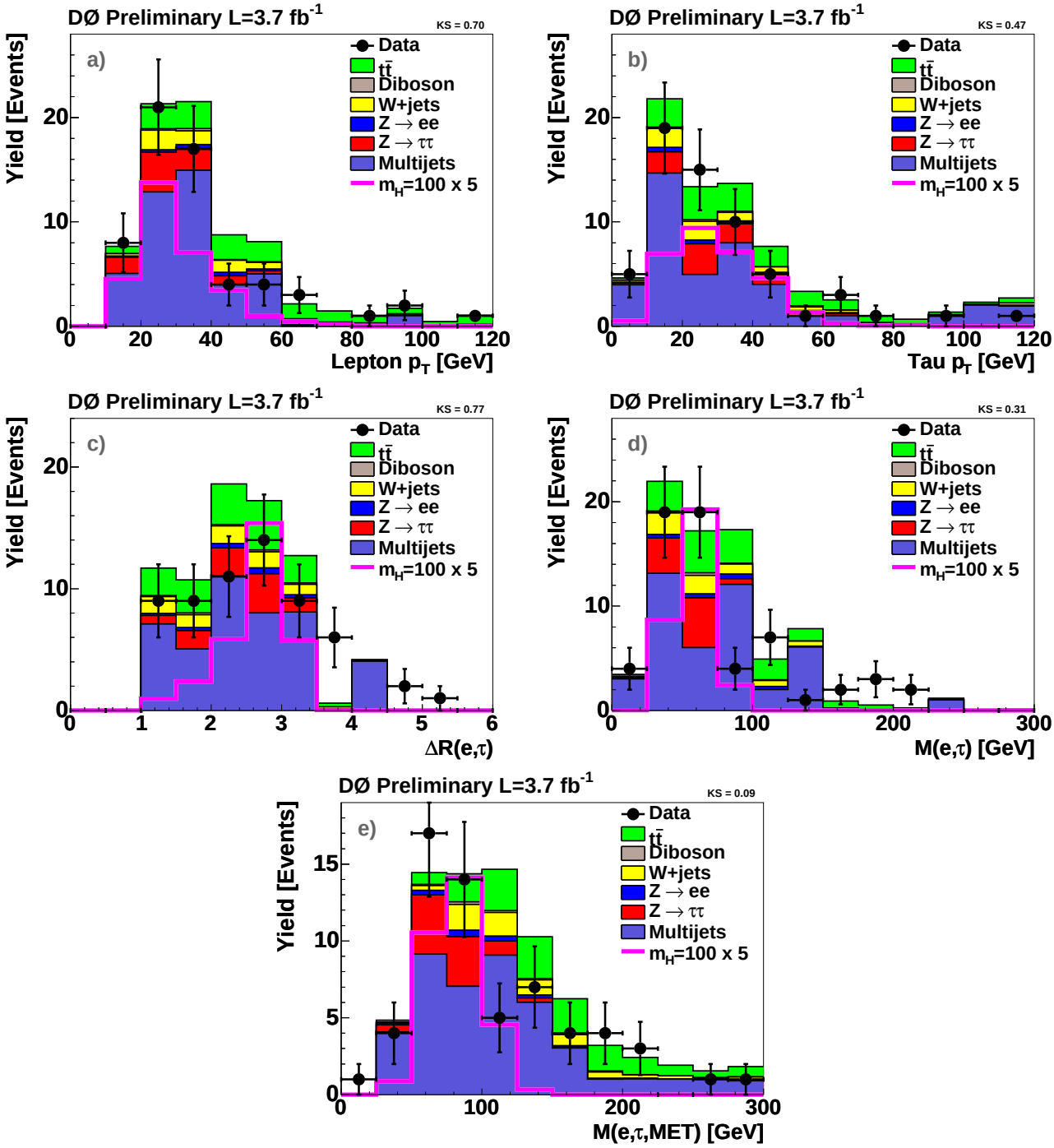

FIG. 4: $LL_{\rm MJ}$ input variables after b-tagging. All tau types are combined.

- The JES, JetID, JetRes and b-tag efficiency uncertainties are calculated by varying the relevant scale or event weight by $\pm 1\sigma$ of their relative errors and recalculating the acceptance. The effect of these new shifted distributions is taken into account in the limit setting, and not just an overall normalization effect.
- The trigger efficiency uncertainty arises from the limited statistics used to derive the turn-on curves in the data for each trigger object. We have estimated this to be a 5% effect.
- The τ identification and NN_τ uncertainty are taken to be 12.5% in type 1, 5.5% in type 2, and 11.8% in type 3.
- The τ energy scale uncertainty is 3% for all types [18].

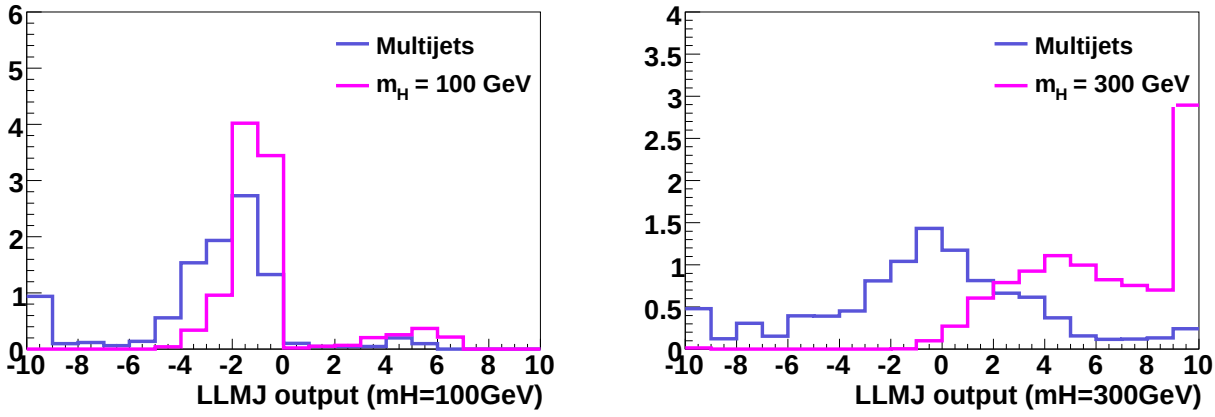

FIG. 5: Separation of the multijet likelihood discriminants for 100 and 300 GeV Higgs boson masses. All areas are normalized to 10.

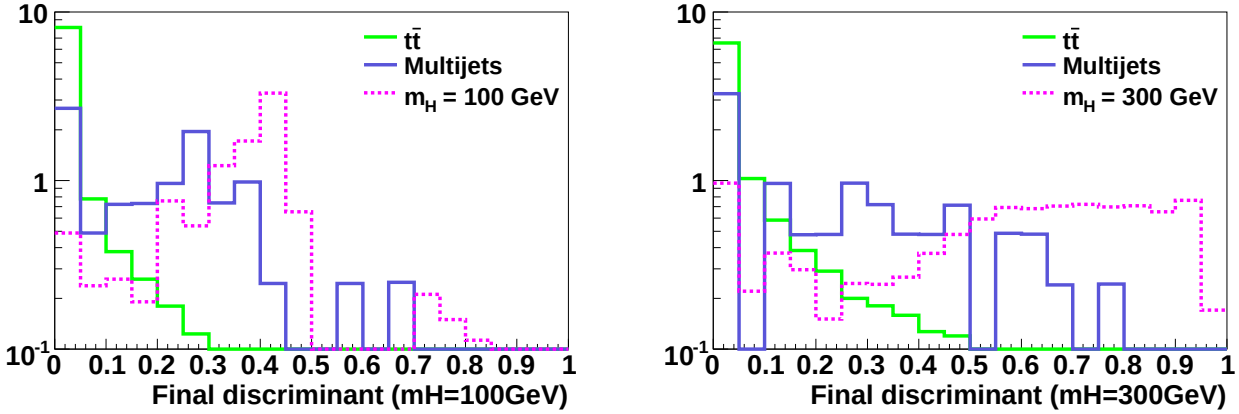

FIG. 6: Separation of the combined discriminant trained for 100 and 300 GeV Higgs boson masses. All areas are normalized to 10.

- The electron identification uncertainty is 8%.
- The luminosity uncertainty is a constant 6.1% [19].
- The multijet uncertainty after b-tagging is taken to be the same as in the muon channel [2]: ranging from 10% to 33% depending on the run period and tau type.
- The uncertainties on the simulated samples normalization are as follows: for Z+lp (light parton) we assign a +2%/-5% uncertainty arising from the NNLO theory uncertainty; for W+lp a 10% uncertainty; for Z+hf and W+hf (heavy flavor: $b\bar{b}$ and $c\bar{c}$) a 30% uncertainty, dominated by the extra heavy quark production scale factor; for $t\bar{t}$ an 11% uncertainty; and for the diboson cross section a 6% uncertainty.

Table IV summarizes the different systematic uncertainties.

VIII. LIMITS AND CONCLUSION

We calculate the cross section limits using a modified frequentist method, the CL_s method, with a log-likelihood ratio (LLR) test statistic [20]. The distributions of the final discriminant outputs (Fig. 7) are used to fit the signal to the data bin by bin, for each tau type as an independent channel and for each signal mass point. To minimize the degrading effects of systematics on the search sensitivity, the individual background contributions are fitted to the data observation by maximizing a profile likelihood function for each hypothesis [21]. Figure 8 shows the expected

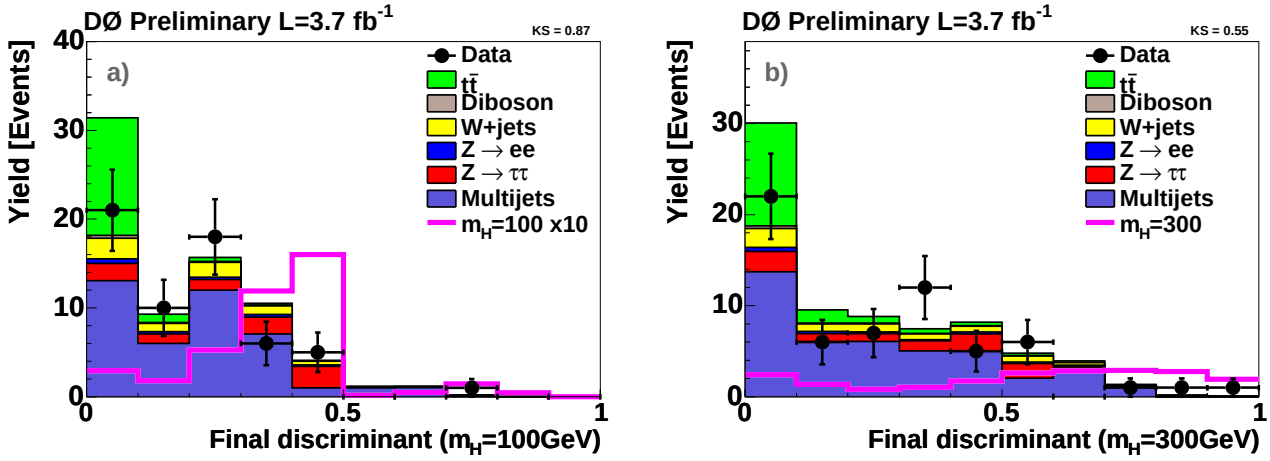

FIG. 7: Combined discriminant distributions trained for 100 and 300 GeV Higgs boson masses.

	Shape systematics				Flat systematics						
Sample	JES	JetRes	JetID	TRF	Trigger	Lumi	τ-ID	τ-ES	e-ID	Multijet	MC σ
Signal	7.4%	6.1%	2.4%	5.6%	5%	6.1%	12.5,5.5,11.8%	3%	8%	–	–
$Z \to \tau\tau$+lp	4.9%	2.1%	0.8%	8.1%	5%	6.1%	12.5,5.5,11.8%	3%	8%	–	$^{+2}_{-5}$%
$Z \to \tau\tau$+HF	3.1%	1.2%	0.8%	5.7%	5%	6.1%	12.5,5.5,11.8%	3%	8%	–	30%
$Z \to$ ee+lp	3.7%	1.6%	0.8%	8.0%	5%	6.1%	12.5,5.5,11.8%	3%	8%	–	$^{+2}_{-5}$%
$Z \to$ ee+HF	2.8%	0.7%	0.1%	5.8%	5%	6.1%	12.5,5.5,11.8%	3%	8%	–	30%
W+lp	5.2%	1.2%	0.6%	7.4%	5%	6.1%	12.5,5.5,11.8%	3%	8%	–	10%
W+HF+lp	3.0%	0.9%	0.1%	5.9%	5%	6.1%	12.5,5.5,11.8%	3%	8%	–	30%
$t\bar{t}$	0.8%	0.2%	0.5%	4.8%	5%	6.1%	12.5,5.5,11.8%	3%	8%	–	11%
Diboson	2.0%	1.8%	1.4%	6.3%	5%	6.1%	12.5,5.5,11.8%	3%	8%	–	6%
Multijet (Run IIa)	–	–	–	–	–	–	–	–	–	18,12,10%	–
Multijet (Run IIb)	–	–	–	–	–	–	–	–	–	33,10,11%	–

TABLE IV: Systematic uncertainties applied to signal and background samples, expressed as a percentage of the nominal value (relative error). The shape systematics are evaluated varying the effect by $\pm 1\sigma$ and using the resulting distributions as inputs into the limit setting. The largest of the positive or negative variation in the total yield is given for those shape systematics to give an idea of the size of the effect. When three numbers appear in one entry, they denote each tau type (1,2,3). A dash (–) means that the systematic on that column is not applied to the sample in that row.

sensitivity and its one and two standard deviations bands, and the observed limit, as a function of neutral Higgs boson mass.

We transform the cross section limits into excluded areas on the $\tan\beta$ vs m_A plane, assumming certain MSSM scenarios: maximal m_h-mixing and no m_h-mixing, and μ=-200 and μ=200 GeV (μ is the Higgs boson mass parameter). FEYNHIGGS v2.6.5 [22] is used to translate the cross section into values of the $\tan\beta$ vs m_A plane. Figure 9 shows the expected and observed limits in the different scenarios.

A combination of these limits with those from other DØ searches in related final states ($\phi \to \tau\tau$, $\phi b \to b\bar{b}b$ and $\phi b \to \tau_\mu \tau_{\rm had} b$) will follow.

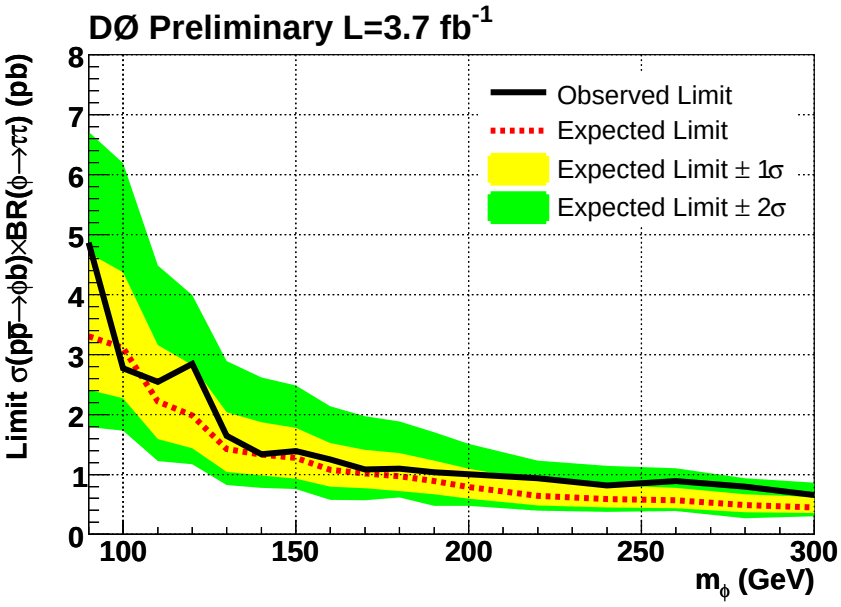

FIG. 8: The limit on the production cross section times branching ratio as a function of Higgs boson mass.

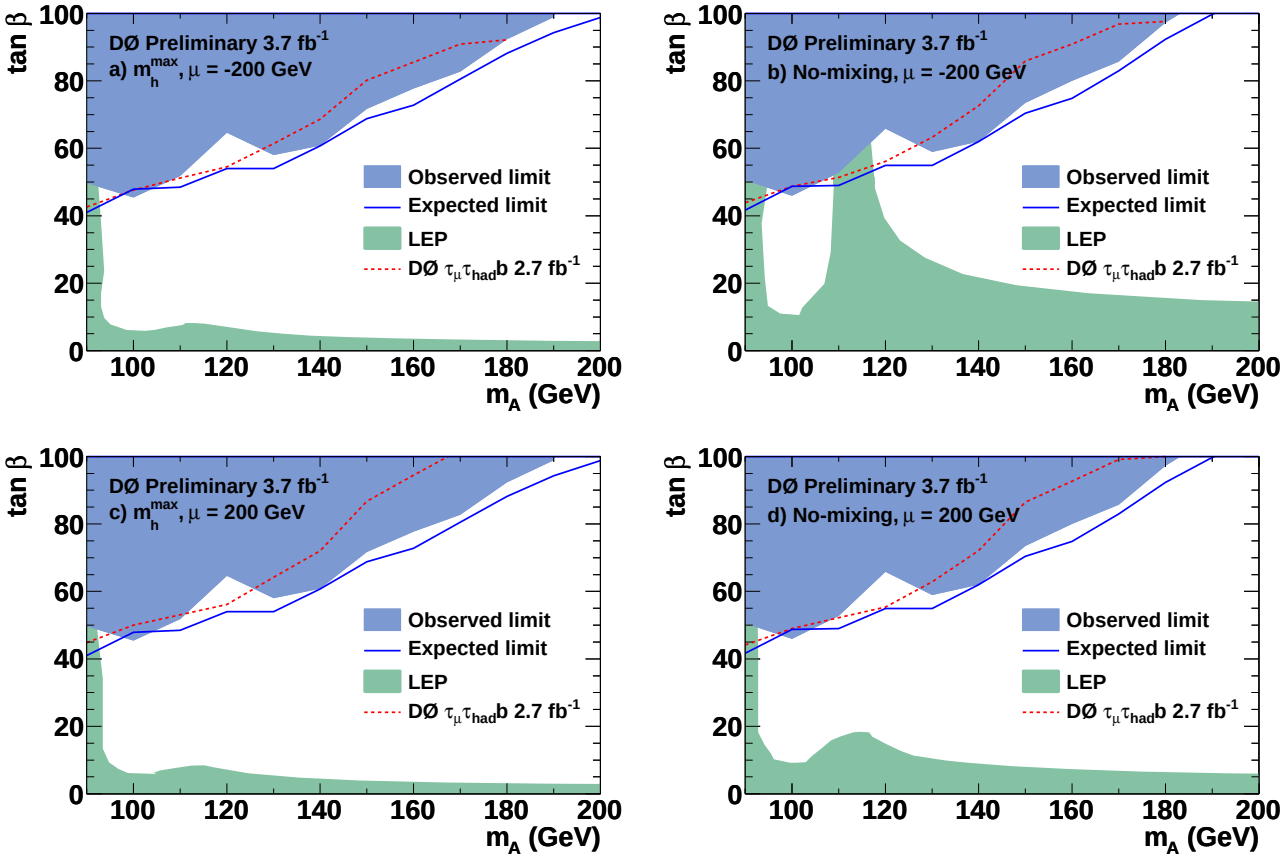

FIG. 9: Limits on $\tan\beta$ vs m_A for the (a) maximal-mixing $\mu < 0$ case; (b) no-mixing $\mu < 0$ case; (c) maximal-mixing $\mu > 0$ case; and (d) no-mixing $\mu > 0$ case. Exclusions from LEP experiments [23], and from the $\phi b \to \tau_\mu \tau_{\rm had} b$ DØ publication [2] with 2.7 fb^{-1} are also shown.

Acknowledgments

We thank the staffs at Fermilab and collaborating institutions, and acknowledge support from the DOE and NSF (USA); CEA and CNRS/IN2P3 (France); FASI, Rosatom and RFBR (Russia); CNPq, FAPERJ, FAPESP and FUNDUNESP (Brazil); DAE and DST (India); Colciencias (Colombia); CONACyT (Mexico); KRF and KOSEF (Korea); CONICET and UBACyT (Argentina); FOM (The Netherlands); STFC and the Royal Society (United Kingdom); MSMT and GACR (Czech Republic); CRC Program, CFI, NSERC and WestGrid Project (Canada); BMBF and DFG (Germany); SFI (Ireland); The Swedish Research Council (Sweden); CAS and CNSF (China); and the Alexander von Humboldt Foundation (Germany).

[1] H.P. Nilles, Phys. Rep. **110**, 1 (1984); H.E. Haber and G.L. Kane, Phys. Rep. **117**, 75 (1985).
[2] V. M. Abazov *et al.* (D0 Collaboration), Phys. Rev. Lett. **104**, 151801 (2010)
[3] V. M. Abazov *et al.* (D0 Collaboration), 5935-CONF (2009)
[4] A. Abulencia *et al.* (CDF Collaboration), Phys. Rev. Lett. **96**, 011802 (2006).
[5] V. M. Abazov *et al.* (D0 Collaboration), Nucl. Instrum. Meth. A **565**, 463 (2006).
[6] S. Abachi *et al.* (D0 Collaboration), Nucl. Instrum. Meth. Phys. Res. A **338**, 185 (1994).
[7] V. M. Abazov *et al.* (D0 Collaboration), Nucl. Instrum. Meth. A **552**, 372-398 (2005).
[8] M. L. Mangano, M. Moretti, F. Piccinini, R. Pittau, and A. Polosa, JHEP **07**, 001 (2003). Version 2.11.
[9] T. Sjöstrand *et al.*, Comput. Phys. Commun. **135**, 23845 (2001). Version 6.409.
[10] J. Pumplin *et al.*, JHEP **0207** 012 (2002) and D. Stump *et al.*, JHEP **0310** 046 (2003). Version 6L1.
[11] Z. Was, Nucl. Phys. B - Proceedings Supplements **98**, 96-102, (2001). Version 2.5.04.
[12] D.J. Lange, Nucl. Instrum. Meth. Phys. Res. A **462**, 152 (2001). Version 9.39.
[13] R. Brun and F. Carminati, CERN Program Library Long Writeup **W5013**, 1993 (unpublished). Version 3.21.
[14] J. Campbell, R.K. Ellis, F. Maltoni, S. Willenbrock, Phys. Rev. D **67**, 095002 (2003). Version 5.6.
[15] R. Hamberg, W.L. van Neerven and T. Matsuura, Nucl. Phys. B **359**, 343 (1991) and errata in **644**, 403; A.D. Martin, R.G. Roberts, W.J. Stirling, R.S. Thorne, Phys. Lett. B **604**, 61-68 (2004).
[16] V. M. Abazov *et al.* (D0 Collaboration), Phys. Lett. B **670**, 292-299 (2009).
[17] V. M. Abazov *et al.* (D0 Collaboration), Nucl. Instrum. Meth. A **620** (2010) 490-517.
[18] V. M. Abazov *et al.* (D0 Collaboration), Phys. Rev. Lett. **101**, 071804 (2008).
[19] T. Andeen et al, FERMILAB-TM-2365-E (2006).
[20] T. Junk, Nucl. Instrum. Meth. Phys. Res. A**434**, 435 (1999). A. Read, CERN 2000-005 (30 May 2000).
[21] W. Fisher, FERMILAB-TM-2386-E.
[22] M. Frank, T. Hahn, S. Heinemeyer, W. Hollik, H. Rzehak and G. Weiglein, JHEP **0702**, 047 (2007). Version 2.6.5.
[23] ALEPH, DELPHI, L3, and OPAL Collaborations, LHWG-Note 2005-01 (2005).
[24] Pseudorapidity is defined as $\eta = -\ln[\tan(\theta/2)]$, where θ is the polar angle with the origin at the center of the detector.
[25] ΔR is the radius of a cone in the azimuthal angle ϕ, and pseudorapidity η. It is defined as $\Delta R = \sqrt{(\Delta\phi)^2 + (\Delta\eta)^2}$